



Water filling in carbon nanotubes with different wettability and implications on nanotube/water heat transfer via atomistic simulations

Alessandro Casto^{a,b}, Francesco Maria Bellussi^b, Michele Diego^a, Natalia Del Fatti^{a,c},
Francesco Banfi^a, Paolo Maioli^a, Matteo Fasano^{b,*}

^a FemtoNanoOptics group, Université de Lyon, CNRS, Université Claude Bernard Lyon1, Institut Lumière Matière, Villeurbanne, F-69622, France

^b Politecnico di Torino, Department of Energy, Corso Duca degli Abruzzi 24, Torino, 10129, Italy

^c Institut Universitaire de France (IUF), France

ARTICLE INFO

Article history:

Received 11 November 2022

Revised 4 January 2023

Accepted 12 January 2023

Available online 25 January 2023

Keywords:

Carbon nanotubes

Water filling

Thermal boundary resistance

Heat transfer

Water

Molecular dynamics

ABSTRACT

The peculiar heat and mass transfer properties of Carbon Nanotubes (CNTs) envision promising applications in nanoengineering and nanofluidic devices, such as heat sinks and desalination membranes. However, a comprehensive understanding of the intertwined effects of mass transfer (entrance and exit of liquid molecules inside CNTs) and heat transfer mechanisms (thermal exchange at the CNT/solvent interface) as a function of the properties of CNT surface is currently incomplete. In this work, we use molecular dynamics simulations to study heat and mass transfer in single wall CNTs with (5,5) and (10,10) chirality immersed in water. We present a sensitivity analysis where, starting from different choices of interaction potentials between CNTs and water molecules, we deduce the corresponding CNT/water wetting parameters, we model fill-in and fill-out water dynamics and arrangement of water molecules at the equilibrium. Spontaneous water entrance into CNTs is examined and a single energy parameter to model water filling is introduced. Secondly, we compute the CNT/water thermal boundary resistance for the different wetting properties. In perspective, this work supports a more rational design of CNT-based devices operating in nanothermal and nanobiological environments.

© 2023 The Authors. Published by Elsevier Ltd.

This is an open access article under the CC BY license (<http://creativecommons.org/licenses/by/4.0/>)

1. Introduction

Firstly synthesized in 1991 [1], Carbon Nanotubes (CNTs) have been widely investigated in the last 30 years, due to their exceptional electrical [2], mechanical [3] and thermal properties [4]. The fields of application of CNTs are vast, ranging from heat transfer enhancement [5,6] to tips of atomic force microscopy [7], from water filtration [8] to nanoactuators [9]. CNTs are also used in water purification processes, due to their strong antibacterial activity against *Escherichia coli* [10] and other bacteria [11], and in desalination processes, where CNT and graphene membranes can be employed for reverse osmosis [12]. Among other aspects, the performance of these CNT-based applications strongly relies on heat and mass transfer phenomena at the interface between the CNTs and surrounding media.

When CNTs are dispersed in water at ambient conditions, the spontaneous water filling may [13,14] or may not occur [15], depending on the CNT diameter and surface characteristics. Water

molecules tend to arrange as ordered layers in the proximity of the CNT surface, thus leading to a specific solid-like water phase, also found in water confined on nanometric distances, which can be accurately studied by Molecular Dynamics (MD) simulations [16–20]. For instance, Alexiadis et al. [21] calculated the density of water inside CNTs, suggesting a correlation between water density and CNT diameter. Pugliese et al. [22] studied the liquid/solid transition of water inside CNTs using the water model Tip4P-ICE [23] for both the liquid and solid phases, observing freezing temperatures higher than in bulk water and dependent on the CNT diameter. Generally, these works make a distinction between hydrophilic or hydrophobic CNTs depending on the water filling capability of CNTs. At the macroscopic level these two concepts are frequently identified by the value θ of the solid-liquid contact angle (CA), which is the internal angle between the tangent to the border of a liquid drop and a liquid-solid interface. A surface is considered hydrophilic in the case of CA smaller than 90° , hydrophobic in the opposite case. In the case of both graphite/water and graphene/water interfaces a wide range of values can be found in the literature [24–26].

Wetting properties also have a strong impact on heat transfer at the interface between CNTs and the surrounding environment. Here, the essential parameter is the Thermal Boundary Re-

* Corresponding author.

E-mail address: matteo.fasano@polito.it (M. Fasano).

sistance (TBR), also known as Kapitza resistance, R_K , which is the resistance to thermal flow at the interface between two materials [27,28]. Indeed, despite the high thermal conductivity of CNTs can improve heat transfer of nanocomposites and nanofluids [29], the overall thermal transfer can be strongly limited by R_K [30]. Analytical predictions of TBR as a result of phonon scattering processes across the interface, such as acoustic mismatch and diffusive mismatch models, may not be accurate at room temperature and atmospheric pressure [31,32]. For this reason, MD simulations were widely adopted to calculate TBR of different nanomaterials, relying on equilibrium or non-equilibrium protocols [33]. Equilibrium MD (EMD) methods deduce TBR through a Green-Kubo formalism observing the fluctuations of energy exchanges across the interface between two materials at the same temperature. A specific EMD approach based on the Laplace transform of the temperature heat flux auto-correlation function was proposed by Alosious et al. [34] to study graphene/water interfaces [35]. They found that R_K is strongly dependent on the water layering in the proximity of the graphene sheets, particularly on the first density peak as also observed by Alexeev et al. [36]. Differently, in Non-Equilibrium MD (NEMD) methods TBR is estimated by inducing a constant heat flux throughout the simulation domain with a steady temperature difference, and analyzing the resulting temperature distribution. NEMD was used to estimate TBR at CNT/water interface [37]. All these methods are subject to possible finite size effect: when the investigated material has dimensions comparable with respect to the mean free path of bulk phonons, the TBR depends on the sample size [38–40]. A third method (used in this work) to calculate the TBR is the Approach to Equilibrium MD (AEMD), which is based on Newton law of cooling for a lumped-capacitance object. In this approach, an initial out of equilibrium condition is applied, by attributing to an object in the simulation domain an initial temperature higher than that of its environment. During the cooling, the temperature relaxation of the object is monitored, and the TBR extracted using heat diffusion equation. Several examples of this method can be found in the literature, mostly applied to solid/solid or filler/polymer interfaces [41–45]. With a refined AEMD approach, Jabbari et al. [46] calculated the R_K at both CNT/water and graphene/water interfaces, examining the effect of CNT diameter and wettability on its value.

To the best of our knowledge, a detailed analysis of the dependence of liquid infiltration (fill-in and fill-out effect of water inside CNT) and of TBR on the wetting properties of CNTs is still lacking. In this work, we proceed through the following steps. We first select different potentials of interaction between CNT surfaces and water molecules, all utilized in the literature, corresponding to different choices of van der Waals interaction strength and equilibrium distances between C and O atoms. For each potential considered, we use MD simulations to calculate the corresponding water/graphene CA, which quantifies the macroscopic wettability between a flat graphene layer and a drop of water. This value corresponds to the intrinsic or Young CA and only depends on the chemical nature of the interface. We then use these values of macroscopic CA to label the different potentials considered, and we compute the fill-in and fill-out dynamics of water into single wall (5,5) and (10,10) CNTs (SWCNTs). This allows to correlate the entrance and exit dynamics (the capability of a CNT to attract water at its interior) to the macroscopic wettability, described by the CA. By a detailed analysis of intramolecular forces in the proximity of the CNT solid-liquid interface, we retrieve a single physical parameter, proportional to the integral of the van der Waals potential in the attractive region, which better correlates, compared to the CA, with the ability of spontaneously attracting water molecules inside the tube. Finally, TBR at the CNT/water interface is calculated for all interaction potentials considered and its dependence as a function of macroscopic wettability (CA) is analyzed.

2. Materials and methods

2.1. Calculation of contact angle

To compute the contact angle θ of the system composed by single layer graphene in water (see Supporting Note S1 for details), we started from Young-Dupré equation [47]:

$$W_{sl} = \gamma_{lv}(1 + \cos(\theta)), \quad (1)$$

being W_{sl} the work of adhesion between liquid and solid phases and γ_{lv} the surface tension of the considered water model [48]. According to the free energy perturbation (FEP) method [49,50], W_{sl} is calculated as the work to transform the solid-liquid interface into a repulsive (non-attractive) interface. The free energy difference between the attractive and repulsive states corresponds to W_{sl} . The variation between the two states is performed via a gradual modification of the interaction energy between the solid interface and the liquid through the variation of the coupling parameter λ :

$$\begin{aligned} W_{sl} &= \frac{1}{S} \sum_{i=0}^{n-1} \Delta_{\lambda_i}^{\lambda_{i+1}} G \\ &= -\frac{1}{S} k_B T \sum_{i=0}^{n-1} \ln \left\langle \exp \left(-\frac{U_{tot}(\lambda_{i+1}) - U_{tot}(\lambda_i)}{k_B T} \right) \right\rangle_i \end{aligned} \quad (2)$$

being k_B the Boltzmann constant, T the temperature, U_{tot} the interaction energy between carbon atoms and water, ΔG the free energy change, S the area in contact with the liquid and λ a coupling parameter, which gradually reduces Lennard-Jones attraction and Coulombic interactions to zero every i -th step for a total number of n steps. Hence, CA is extracted from Eq. 1 after calculating W_{sl} using Eq. 2 over the MD trajectory simulated with the considered Lennard-Jones interaction potential and introducing the value of γ_{lv} obtained in the literature, independent of the CNT/water interaction potential [48].

2.2. Water mass transfer dynamics

For each set of solid-liquid van der Waals interactions, the number of water molecules inside the CNT is counted. Firstly, we studied the filling dynamics: in the initial condition, the empty CNTs are placed in a box filled with water molecules, and the spontaneous liquid filling is monitored as a function of time in an equilibrium environment corresponding to the different wetting parameters. To observe the inverse dynamics, water molecules are placed inside CNTs with an initially highly hydrophilic condition. Then, the specific interaction potential is introduced, and the exit dynamics monitored until equilibrium is achieved.

2.3. Thermal boundary resistance

In the AEMD method, R_K is evaluated observing the time evolution of the average particle temperature T_p from an initial non-equilibrium state (the particle is heated up with respect to the surrounding ambient temperature T_a) to the overall thermal equilibrium. Under the assumption of a sub-unitary Biot number (lumped capacitance approximation) and constant water temperature, the time dependent temperature difference $\Delta T = T_p - T_a$ evolves as:

$$\Delta T(t) = \Delta T(t=0) \exp(-t/\tau), \quad (3)$$

where the exponential decay time is

$$\tau = R_K \frac{C}{S}, \quad (4)$$

being C the heat capacity of the particle and S the heat exchange surface [51]. However, the lumped-capacitance approximation is

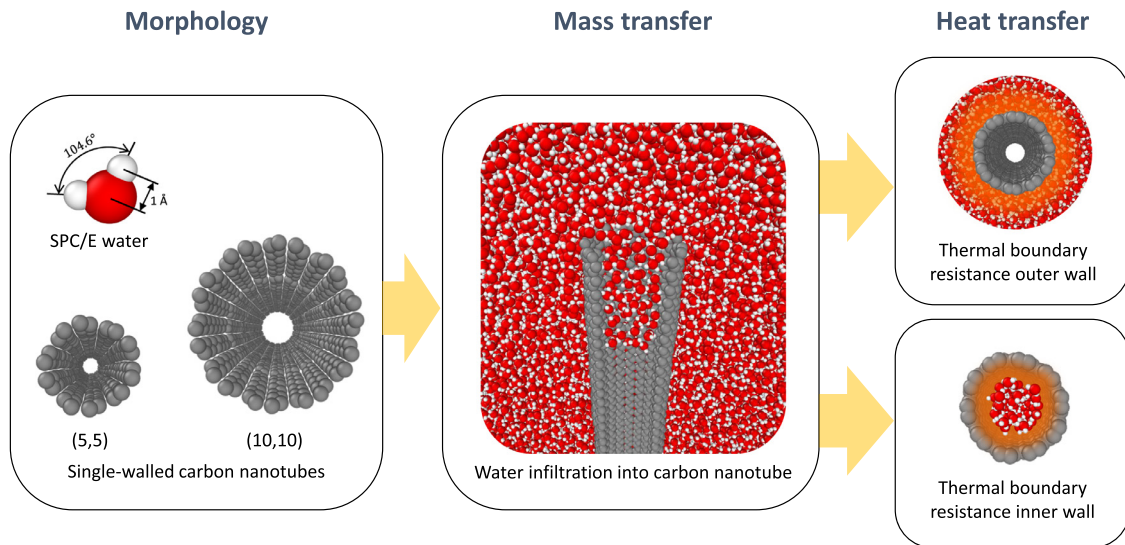


Fig. 1. Pictorial representation of the simulation workflow performed. On the left, the water model adopted (SPC/E) and the two CNTs used ((5,5) and (10,10) chiral index). In the middle, a sketch of water filling of the CNTs is shown. On the right, configurations used for evaluation of the TBR at the outer and inner wall interfaces with water are shown.

valid only when the thermal resistance across the interface is dominant, with negligible temperature gradients both in the CNT and in the surrounding medium. To overcome these limitations, the TBR at CNT/water interface was here calculated following the AEMD approach reported by Jabbari et al. [46]. In this case, the heat capacity of the CNT and the temperatures profiles of CNT and water close to the CNT are not needed. After the nanoparticle is initially heated up to a higher temperature with respect to the surrounding environment, the variation of the total energy concomitant with nanoparticle cooling can be expressed as

$$\frac{\partial E_t}{\partial t} = -\frac{T_p - T_a}{R_K/S}. \quad (5)$$

The variation in total energy of the CNT is then equal to the time integral of the heat flux between the nanoparticle and water:

$$E_t = -\frac{S}{R_K} \int_0^t (T_p - T_a) dt + E_0 \quad (6)$$

with E_0 constant background energy. As T_p , T_a and E_t can be deduced for each simulation time, it is then possible to compute R_K from the best fitted value of $-S/R_K$. T_a is computed here considering only water molecules in the proximity of CNT surface (either inside and in the outer region), therefore not accounting for the thermal resistance of bulk water itself. For all the simulations we set the heat transfer surface S between the two phases as the surface of the cylindrical region with diameter and length of the CNT. Notice that the value of R_K measured via AEMD can be associated to a temperature range between T_p and T_a .

2.4. Computational details

MD simulations were carried out by means of LAMMPS [52]. Fig. 1 shows an overview of the simulation protocol. We performed all simulations with a 1 fs time step and Verlet integration scheme. We adopted the Tersoff force-field [53] to model carbon-carbon interactions for both the CNTs and graphene sheets, and the three-point charge SPC/E force-field [54] to describe water molecules. We chose a cutoff of 1 nm to compute the non-bonded interactions, and the PPPM method with 10^{-4} accuracy for the long range electrostatic interactions [55]. In particular, in accordance to the water model, carbon-hydrogen interactions are neglected and interactions between carbon atoms and oxygen atoms of water are

modeled using a Lennard-Jones potential:

$$U_{LJ}^{CO}(r) = 4\epsilon_{CO} \left[\left(\frac{\sigma_{CO}}{r} \right)^{12} - \left(\frac{\sigma_{CO}}{r} \right)^6 \right]. \quad (7)$$

We employed 7 different pairs of ϵ_{CO} and σ_{CO} Lennard-Jones parameters (see Table 1), taken from Werder et al. [24–26]. They mimic the dispersion of CNT/water wetting properties that could arise from different surface functionalizations [56,57] and defects [58,59]. We also used three potentials calculated starting from SPC/E model [54] and OPLS-AA force-field [60] for water and carbon respectively and applying geometric, arithmetic and sixth power mixing rules (see Supporting Note S2 for details). We generated the initial CNT topology with VMD [61] and the input LAMMPS data and files with Moltemplate [62] (see the code available at Reference [63] for details). SWCNTs with 10 nm length and (5,5) and (10,10) chirality were simulated, corresponding to diameters of 0.687 nm or 1.375 nm respectively.

First, we placed the empty SWCNTs in a box filled with water molecules, to observe the possible liquid filling of the CNT at equilibrium conditions. All the simulations were performed at 1 bar and 290 K. The system was equilibrated through a NPT simulation (Nose-Hoover thermostat and barostat [64], with time constants equal to 100 fs and 1000 fs, respectively) up to 2 ns for the (5,5) and 2.5 ns for the (10,10), followed by a NVT run (Nose-Hoover thermostat, with time constant equal to 100 fs) up to 0.5 ns. These simulations are replicated up to three times for each corresponding CNT/water potential interaction. To compute the fill-out dynamics, we started from the configuration with the highest wettability and thus water filling into the CNT at equilibrium conditions, and we performed NPT simulations of liquid expulsion for up to 2.5 ns after modifying Lennard-Jones parameters. During simulations, we calculated the water density profiles in the (5,5) and (10,10) systems with radial concentric bins of 0.025 nm width along the main axis of the CNT.

To estimate the TBR at the inner and outer CNT/water interfaces we realized two different systems: one with water molecules only inside the CNT, another with water only outside (Fig. 1). These two setups helped us in discriminating between the (possible) different TBR at the inner and outer CNT surfaces. These setups were made starting from equilibrated configurations and then removing water molecules from the inner/outer regions. After that, to avoid spon-

taneous entrance or exit of water molecules at the head and tail regions of the CNT, we applied periodic boundary conditions along the main axis of the CNT (see Supporting Note S3). Periodic conditions also allow us to simulate the heat flux from the CNT to water selectively in the radial direction. We equilibrated the periodic systems for 500 ps in NVT ensemble, with the same thermostat detailed above. Subsequently, we induced a radial heat flux setting the temperature of carbon atoms at 400 K while that of water molecules at 290 K during a 300 ps NVT simulation. Lastly, we monitored carbon energies E_p and temperatures T_p , T_a in a NVE simulation for 1 ns (see Supporting Note S4). When calculating the external TBR, we stored the water temperatures for cylindrical regions with radii of 1.250 nm ((5,5) CNT) or 1.775 nm ((10,10) CNT) from the axis of the CNT. These fluid regions correspond to those of nanoconfined-like water.

Finally, we performed FEP calculations with the soft style modification for Lennard-Jones and Coulombic interactions in LAMMPS [65]. For this case, we simulated a box of 1000, initially equilibrated, SPC/E water molecules with a 3.2 nm x 3.2 nm single graphene sheet, while monitoring the potential energy. The λ parameter was incrementally decreased each 1 ns, passing from 1 to 0 over a 20 ns NVT simulation. We remark that the CA evaluated on flat graphene surfaces corresponds to the intrinsic or Young CA, which allows to uniquely define the chemical nature of the interface. The possible effects of roughness or curvature can be in principle taken into account adopting analytical (i.e., Wenzel [66] and Cassie-Baxter [67]) or numerical (i.e., atomistic [68,69] or multi-phase [70]) models, where the intrinsic CA can be adopted as boundary condition at the solid-liquid interface.

3. Results and discussion

3.1. Choice of potential and computation of contact angles

The measured CAs (θ) for graphite and graphene corresponding to the different choices of Lennard-Jones parameters are summarized in Table 1. For the 7 different combinations of σ_{CO} and ϵ_{CO} taken from Werder et al. [24] we reported the CAs computed by the authors for the graphite/water interface and the CAs computed here for the graphene/water interface, as explained in Section 2.1. Note that in the paper cited the graphite is modeled as two piled sheets of graphene. For the three σ_{CO} and ϵ_{CO} pairs obtained by combining the SPC/E water model and OPLS-AA carbon force-field, only the graphene/water CA is reported as calculated here.

Differences in the CAs between the current work and previous results from Werder et al. [24] could be explained both because of the different structures taken into account (graphene vs. graphite, where the presence of an additional carbon layer generally enhances surface hydrophilicity, as also observed by Chiricotto et al. [71]), and also by the distinct methods employed in the two works to calculate CA. The method adopted in this work is based on the evaluation of the free energy difference due to the progressive tuning off of the interaction parameter ϵ_{CO} between solid and liquid. Consequently, such energy variation is only dependent on the cross interaction parameters between the two different phases in contact. As also pointed out by Leroy et al. [72], who investigated the wetting of graphene layers with different water models using the FEP approach, the water CA evaluated with this method results to be almost independent on the water model adopted. In the case of the droplet density profile model employed by Werder et al., instead, the surface density profile approach may result dependent on the water model adopted, due to the difference on surface tension, especially when the system simulated is not dimensionally sufficient to avoid finite size effect. Nevertheless, the wetting behaviours of graphene and graphite result consistent between each

Table 1

Lennard-Jones parameters for carbon/oxygen interactions and corresponding graphite/water and graphene/water CAs computed from MD simulations. σ_{CO} and ϵ_{CO} are taken from Werder et al. [24], in the lines where the graphite/water CA is indicated, and from SPC/E water model [54] and OPLS-AA aromatic carbon [60] for the other cases, using ^a Geometric, ^b Arithmetic, and ^c Sixth power mixing rule. Graphite/water CAs are taken from the work of Werder et al. [24]. Graphene/water CAs are obtained in this work by means of the Free Energy Perturbation approach and the Young-Dupré equation. The color code adopted in the following figures is also indicated.

	σ_{CO} [nm]	ϵ_{CO} [kcal/mol]	θ - Graphite	θ - Graphene
	0.3190	0.1498	29.4°	45.74°
	0.3190	0.1348	50.7°	61.97°
	0.3190	0.1199	69.9°	75.69°
	0.3352	0.1043	-	77.84° ^a
	0.3358	0.1043	-	78.56° ^b
	0.3190	0.1049	85.9°	89.07°
	0.3385	0.0984	-	94.07° ^c
	0.3190	0.0937	95.3°	97.74°
	0.3190	0.0749	109.2°	113.39°
	0.3190	0.0450	143.3°	136.12°

other, with values ranging from 29.4° to 143.3° according to the different C-O interactions modelled.

3.2. Water filling of CNTs

Fig. 2 shows the entrance/expulsion of water molecules into/from CNTs for both the (5,5) and (10,10) systems. The overall number of water molecules inside the CNT was detected during the NPT simulation for the two CNTs as a function of the water physical filling and emptying time starting from void (a,c) or filled (b,d) CNTs. Three distinctive color codes are used. Red to yellow curves correspond to different values of ϵ_{CO} and same σ_{CO} , green curves to different σ_{CO} and same ϵ_{CO} (different than the ones used before), and blue for ϵ_{CO} and σ_{CO} which are different than all previous parameters (see Table 1).

For the (5,5) CNT, we observe spontaneous entrance of water (see Fig. 2a) in the hydrophilic regime for $\theta \leq 75.69^\circ$. The average maximum number of water molecules accessing the CNT volume is equal to 37 ± 1 in the most hydrophilic configuration ($\theta = 45.74^\circ$). Instead, for all the systems with $\theta \geq 77.84^\circ$ the stable number of infiltrated water molecules is equal to 0, hence, the CNT results to be internally hydrophobic. Equivalent results are obtained in the case of expulsion dynamics (see Fig. 2b), no hysteresis is observed during successive entrance/expulsion processes.

For the larger (10,10) CNT, water molecules can enter the tube for $\theta \leq 78.55^\circ$ (see Fig. 2c). For $\theta = 89.07^\circ$, on the contrary, the number of water molecules into the CNT is small and unstable. For a CA equal to 94.07° , water molecules are again free to access the carbon CNT reaching a stable number. For larger CAs, the CNT is hydrophobic and molecules do not enter. Such water filling behaviour is non-monotonic with respect to θ , highlighting that – when it comes to spontaneous water filling of CNTs at ambient conditions – the equivalent graphene CA may not be the most adequate parameter to interpret results. Considering the expulsion phenomenon (see Fig. 2d), we observed spontaneous exit of water for all the configurations with $\theta \geq 113.39^\circ$, while for values $\theta \leq 97.74^\circ$ the number of water molecules inside the CNT is large and stable. By comparing the fill-in and fill-out dynamics (Fig. 2c and Fig. 2d), we observe that for intermediate values of CA, equal to 89.07° and 97.74° , the number of water molecules at equilibrium depends on the initial configuration (i.e., water-filled or void): if the (10,10) CNTs are initially void (as in Fig. 2c) they remain void,

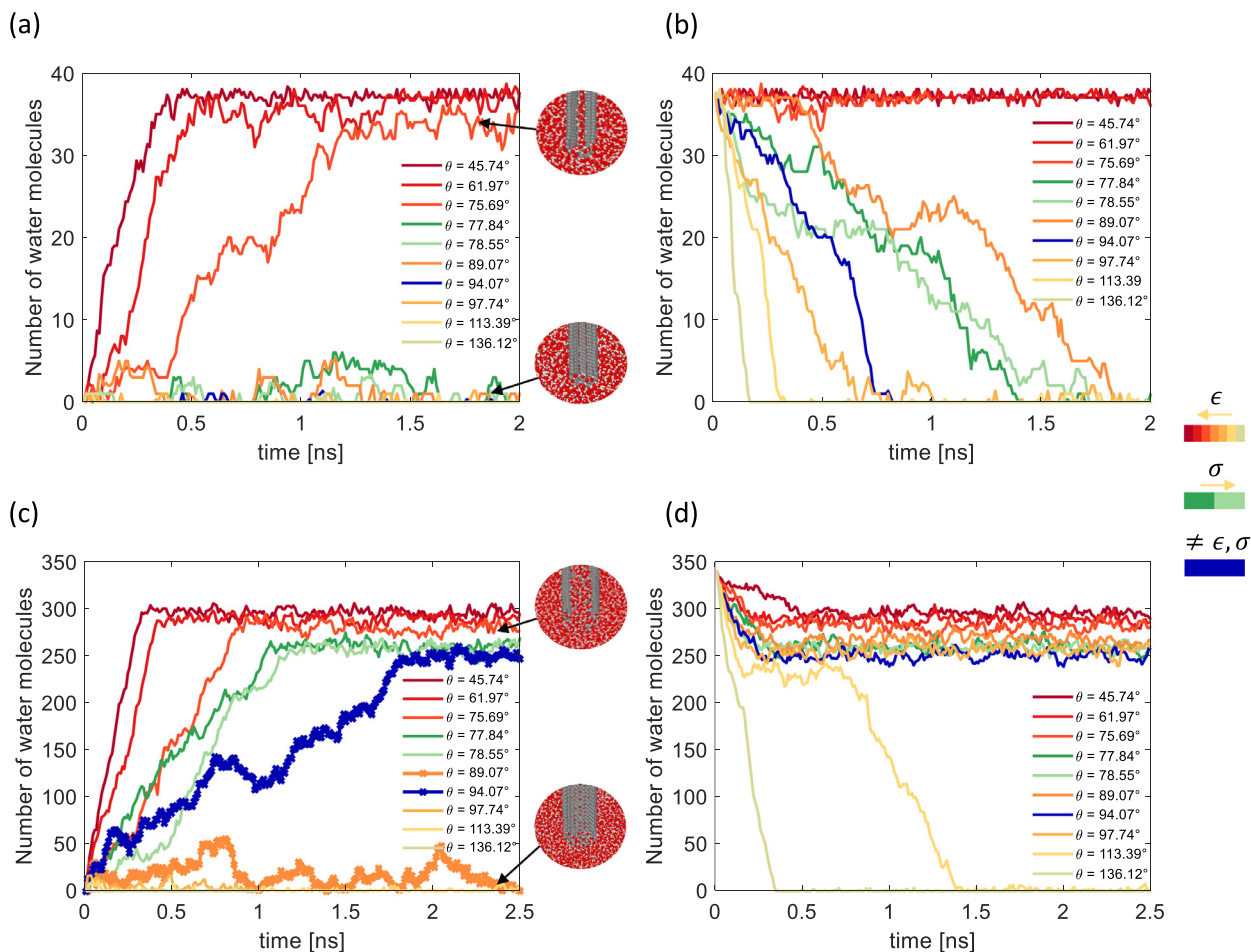


Fig. 2. Number of water molecules inside the CNT over time for different CA values. a) Water infiltration into (5,5) SWCNTs initially empty, and b) exit from completely filled-in condition. c) and d) same for (10,10) SWCNTs. The small images are frames of the equilibrated MD simulation. The CAs are computed using Lennard-Jones parameters of Table 1. Yellow to red lines indicate a variation of ϵ_{CO} with σ_{CO} fixed. Green lines indicate a variation of σ_{CO} with ϵ_{CO} fixed. The blue line corresponds to two different values of ϵ_{CO} and σ_{CO} .

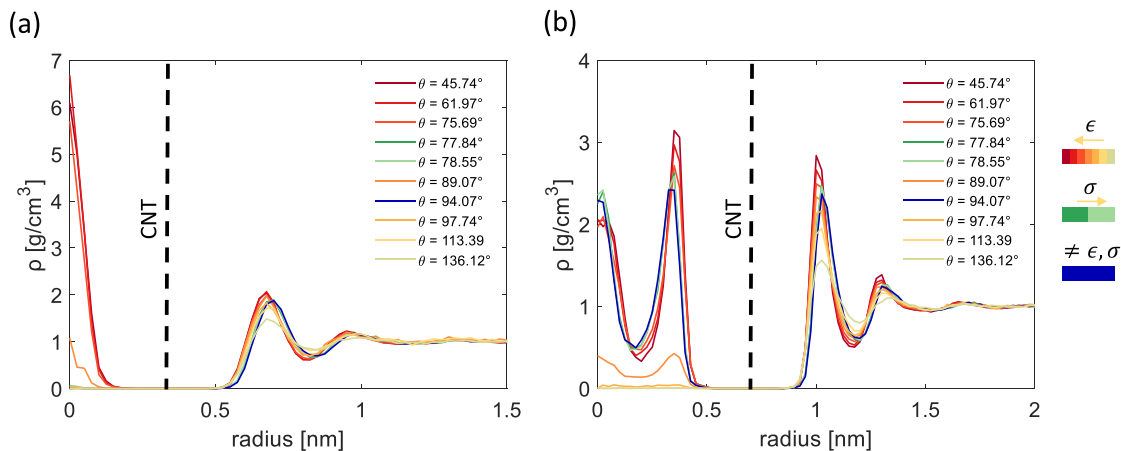


Fig. 3. Water density profile along the axis of the carbon nanotube for a the (5,5) (a) and (10,10) (b) systems at equilibrium starting from empty conditions. The dotted lines represent the position of carbon atoms of the CNT.

while the opposite is observed for the initially filled (10,10) CNT (Fig. 2d). For all the other cases, equilibrium is reached regardless of the initial configuration. In particular, 293 ± 4 molecules of water on average enter the CNT in the most hydrophilic configuration (small CA).

As shown in Fig. 3, for the two CNT morphologies with initial empty conditions, a large total amount of water molecules inside the CNT at equilibrium (Fig. 2a and c) is associated with their large densities at the center of the CNT.

In the case of (5,5) CNT (Fig. 3a), water molecules inside the CNT are arranged in a single-row configuration with a single hydrogen bond between each pair of molecules. A similar single-row structure was also theoretically predicted by Pascal et al. [73] and experimentally observed by Ma et al. [74] in iced CNTs. A radial bilayer-like configuration of water molecules is expected for the (10,10) CNT, with peak densities on the CNT axis and for radius around 0.38 nm. Interestingly, the density of water molecules outside CNTs displays for both morphologies density peaks which are higher for smaller CAs, corresponding to larger hydrophilicity (this is particularly visible in Fig. 3b for the (10,10) CNT). This result indicates that a larger hydrophilicity induces a denser layer of water outside the CNT, as also reported in previous studies [36,46]. Here again, by carefully comparing water densities inside the (10,10) CNT for different CAs (Fig. 3b), the same non-monotonic dependence as in Fig. 2c is observed, water density for $\theta = 89.07^\circ$ being much smaller than the one for $\theta = 94.07^\circ$. On the contrary, the θ -dependence of water density outside (10,10) CNTs is more regular. These results show that the CA may not be the most suitable parameter to quantitatively predict the CNT filling dynamics (or equivalently, the number of water molecules inside CNTs at equilibrium), particularly in the transition between the hydrophilic-hydrophobic behaviour for the larger CNT. In the following, we propose a new physical parameter more pertinent to account for the interaction energy between carbon and water atoms.

3.3. Mechanistic interpretation of CNT water filling

The entrance of water molecules into the CNT is highly dependent on the wettability of the CNT surface. Starting from Lennard-Jones interaction potential between carbon and oxygen in Eq. 7 and summing over all C atoms, the total energy of an O atom in the plane at the CNT mid-length and at distance r from CNT axis can be analytically expressed as:

$$U(r) = \sum_{i=1}^N 4\epsilon_{CO} \left(\frac{\sigma_{CO}^{12}}{\left((R_{CNT} \cos(\alpha_i) - r)^2 + R_{CNT}^2 \sin^2(\alpha_i) + h_i^2 \right)^6} - \frac{\sigma_{CO}^6}{\left((R_{CNT} \cos(\alpha_i) - r)^2 + R_{CNT}^2 \sin^2(\alpha_i) + h_i^2 \right)^3} \right). \quad (8)$$

Considering the planar surface which cuts the CNT at mid-length, X and Y define the reference frame of the cross-section with center in A in the axis of the CNT (see Fig. 5), α_i is the angle of the center of mass of the i -th carbon atom and the X axis, r is the radial distance of the O atom from the CNT axis, h_i is the longitudinal distance between the i -th carbon atom and the cross-sectional plane, R_{CNT} is the radius of the CNT and N is the total number of carbon atoms.

Fig. 4a and c show $U(r)$ (Eq. 8) corresponding to different σ_{CO} and ϵ_{CO} pairs tested in this work (cf. Table 1). The number of water molecules attracted inside CNTs is proportional to the integral of $U(r)$ in the volume accessible to water, i.e. the part of the cross-sectional plane where $U(r) < 0$, which ranges from $r = 0$ to the point where $U(r) = 0$. This integral, limited to the attractive region, where $U(r) < 0$, and normalized over the surface of the cross-section of the CNT, writes:

$$\beta = \frac{1}{\pi R_{CNT}^2} \int_0^{R_{limit}} U(r) 2\pi r dr, \quad (9)$$

being $U(r = R_{limit}) = 0$. The values of β for all the considered CNT configurations are listed in the Supporting Note S5. The number of water molecules filling the CNT at steady state (i.e., the asymptotic values in Fig. 2), is shown in Fig. 4b and d for the (5,5) and (10,10)

CNTs, respectively, as a function of β . The same graph is reported as a function of the graphene CA in Supporting Figure S4.

As expected, β is affected by the values of both ϵ_{CO} and σ_{CO} . In the $U(r)$ expression above (Eq. 8), ϵ_{CO} is a proportionality factor and only affects the overall amplitude of the interaction potential with no modification of its profile (see red to yellow curves in Fig. 4a and c). Note that $U(r)$ has a minimum around $r = 0.38$ nm for the (10,10) CNT (Fig. 4c) while the minimum is at $r = 0$ nm for the (5,5) CNT (Fig. 4a). The minima of the potentials inside the CNT correspond to the position of the density peaks as shown in Fig. 3 (in the axis of the CNT for (5,5) and near 0.38 nm for the (10,10)). Variations of σ_{CO} , on the contrary, modify the shape of the potential. As it may be seen by an accurate comparison of the two green curves for the (5,5) CNT (Fig. 4a), the $U(r) = 0$ zero-crossing point shifts to smaller r when increasing σ_{CO} , thus reducing the attractive region. $U(r)$ interaction potentials indicated by green and blue curves ($\theta = 77.84^\circ, 78.55^\circ$ and 94.07°) globally correspond to large values of σ_{CO} , higher than the one corresponding to red to yellow curves. Their horizontal shifts with respect to the latter is manifest. The shift towards more hydrophobic condition with increasing σ_{CO} clearly shows up when plotting β as a function of CA, as in Supporting Figure S5a for the (5,5) CNT. In the case of (10,10) CNT (Fig. 4c and Fig. S4b), the horizontal shift with increasing σ_{CO} is accompanied by a deepening of $U(r)$ potential well, resulting in smaller deviations from a linear β over θ dependence (Supporting Figure S5b).

Results show that β is more precise than CA in characterizing the water filling mechanism of CNTs at ambient conditions for different carbon-water interaction energies – thus wetting properties. In particular, a monotonic curve appears at the transition between hydrophilic-hydrophobic response of the (10,10) CNT, differently from what observed as a function of CA (Supporting Figure S4). A threshold behavior appears around $\beta = -0.15$ kcal/mol and $\beta = -0.5$ kcal/mol for the (5,5) and (10,10) CNT respectively, the number of molecules at equilibrium being large and constant for smaller β and 0 for larger ones. The sharp transition around these points is dependent on the state of water close to the CNT, as investigated by Pascal et al. [73]. In this work, we do not investigate the state of water any further, but we reckon that this can be the starting point for following contributions in the future.

In Supporting Figure S6, we also show the $U(r)$ in the outer surface computed with Eq. 8. In this case, the shape of the potentials are mirrored with respect to the CNT. Hence, the previously reported conclusions regarding the effect induced by variations of σ_{CO} are mirrored, i.e., an increase of σ_{CO} (green and blue curves) is followed by an increase of the equilibrium position. On the contrary, we report the deepening of the potential well with the increase of ϵ_{CO} similarly to Fig. 4a-c. Also, the minima of the potential correspond to the first density peaks in the outer region (around 0.65 nm for the (5,5) CNT and 1 nm for the (10,10) CNT).

As a conclusion, CAs computed for graphene sheets are – in general – a good descriptor of the water filling behaviour of the CNT except at the sharp hydrophilic-hydrophobic switch, where curvature plays a significant role and thus β appears as a more comprehensive physically justified parameter to describe such wetting mechanism.

3.4. Thermal boundary resistance

Fig. 6 shows the TBR between the inner or outer surface of CNT and water. For the inner CNT/water interface, TBR was calculated only for the configurations with a stable number of water molecules filling the CNT at equilibrium, i.e. $\theta \leq 94.07^\circ$ for the (10,10) CNT. The TBR at the inner CNT/water interface of the (5,5) CNT was not computed due to the intrinsically low number of water molecules (around 30) and thus not significant statistics.

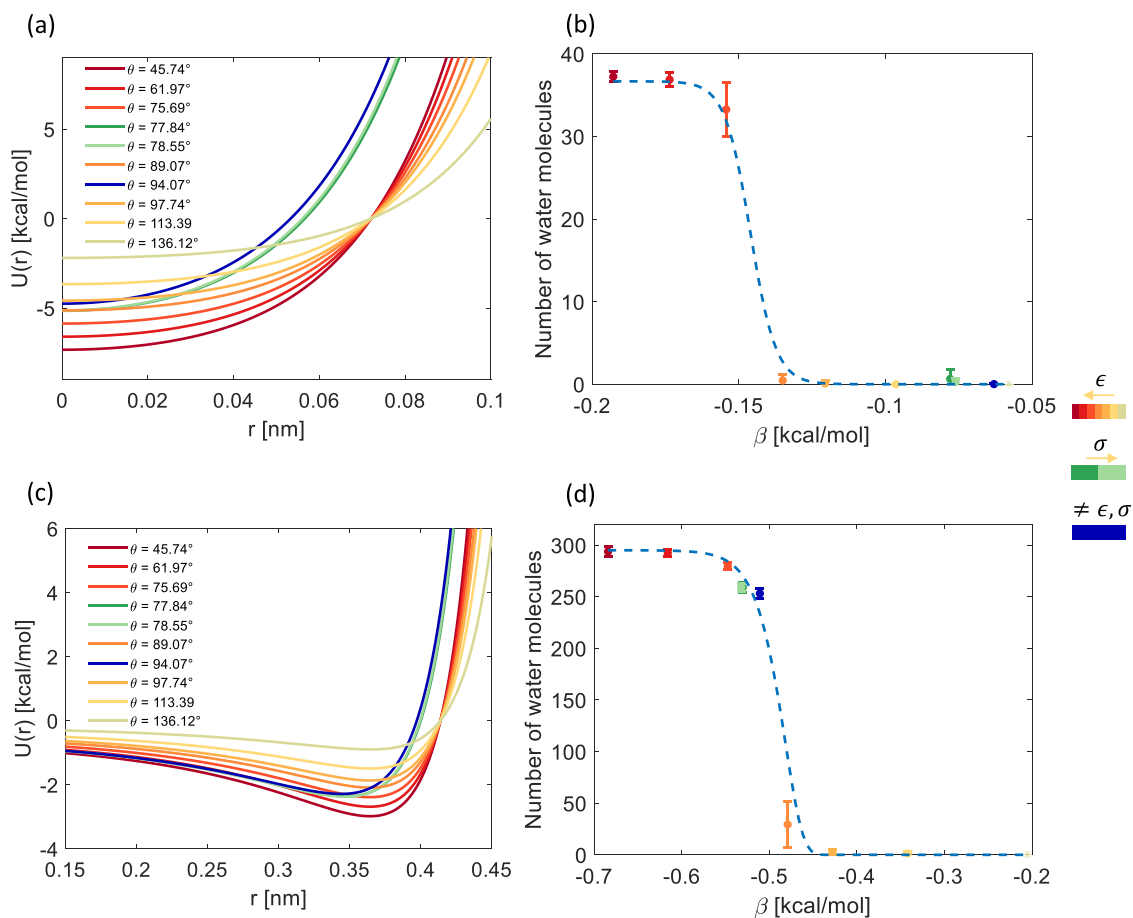


Fig. 4. a) Interaction potentials between all the C atoms of a (5,5) CNT and an O atom at position r in the mid-length cross-section. b) Number of water molecules inside the (5,5) CNT at equilibrium starting from void condition as a function of wettability parameter β . c) and d) same for a (10,10) CNT. The dashed lines in b) and d) are guides for the eye.

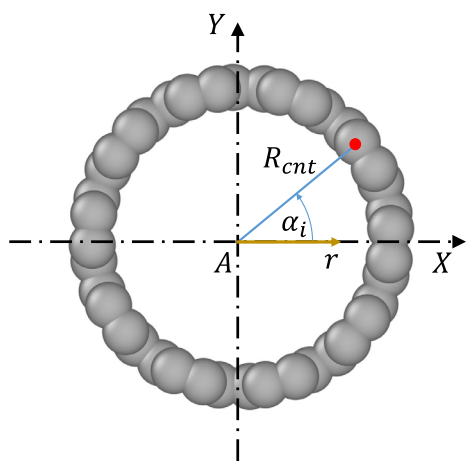


Fig. 5. Cross-section of a (10,10) CNT.

In this analysis, CA is used to describe wettability. This choice is made on the base of: firstly, the variability of the TBR (Fig. 6a) is large enough that there is no significant difference in the dependence using β instead of CA for the x -axis; secondly, the β parameter is not defined at the external surface of the CNT (Fig. 6) since it is used to describe spontaneous filling. We recall that the

fluid region considered to compute R_K is within a radial distance of 1.250 nm and 1.775 nm from the axis of the (5,5) and (10,10) CNTs, respectively. These distances are chosen considering the nanoconfined water close to the CNT as shown in the density profiles in Fig. 3.

With regards to the TBR at the outer CNT/water interface, values in the range $4\text{--}12 \times 10^{-8} \text{ Km}^2/\text{W}$ were found for the smaller (5,5) CNT, while $3\text{--}8 \times 10^{-8} \text{ Km}^2/\text{W}$ for the (10,10) one. Results show two main effects. At first, the dependence of the TBR with the dimension of the CNTs: for lower radius of the CNT a higher TBR is observed. A similar trend of TBR with CNT radius was reported in the MD simulations by Alosious et al. [75], where this dependence was attributed to the ratio between the number of water molecules in a region of fluid close to the CNT and its radius. The second effect is that higher surface wettability (i.e., lower CA) is generally responsible for a lower thermal boundary resistance. Low CA values indeed lead to higher water density peaks in the proximity of CNT surface (see Fig. 3) which induce a better heat conduction. Limited differences of TBR between the inner and outer CNT/water interfaces are recorded. Similarly, Alexeev et al. [36] demonstrated that, in the case of a planar surface (graphene), the TBR is proportional to the first density peak of water close to the surface. Equivalent discussions were also reported by Jabbari et al. [46], where surface wettability was responsible for an increase in the first density peak of water in the proximity of CNT surface. This behaviour was observed for other nanoparticles as well, e.g. at the silicon-water interface [76,77]. Moreover, for nanoparticles with spherical geometries, similar variations of

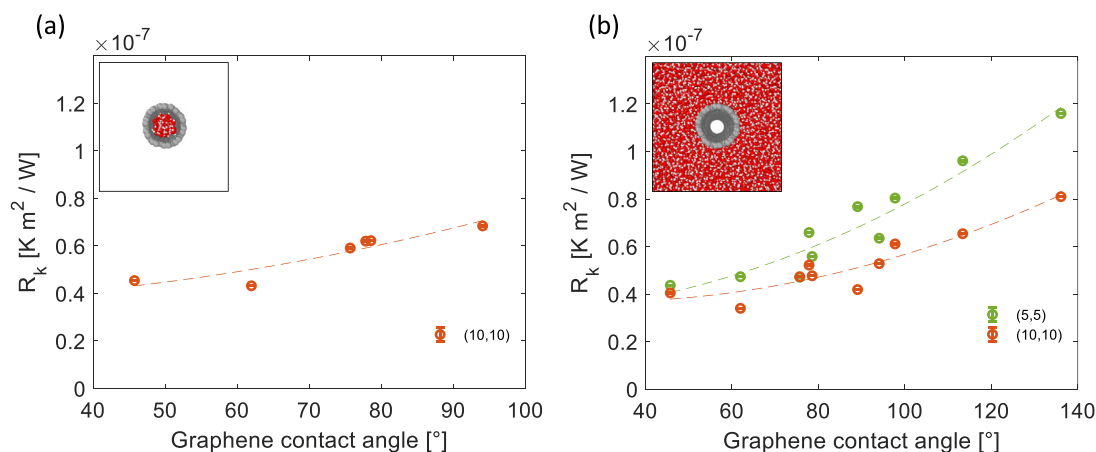


Fig. 6. TBR at the inner wall-water interface for the a) (10,10) CNT, and b) at the outer wall-water interface for the (5,5) and (10,10) CNTs. Dashed lines are guides for the eye.

the TBR were previously found either with respect to the change of wettability [78,79] and the size of the nanoparticle [79]. In accordance with these works, results summarized in Fig. 6 indicate that both CNT wettability and curvature have an effect on the TBR. They both influence the nanoconfined water structure and thus heat transfer at the solid-liquid interface. Indeed, hydrophilic and large CNTs show a better interfacial heat transfer, with negligible differences between inner and outer CNT interfaces. With reference to Fig. 3 it is possible to conclude that the reduction of the TBR is caused by the presence of highly structured and dense solid-like water in the vicinity of the solid structure (hydrophilic conditions), which ease heat transfer at the interface.

4. Conclusions

In this work we used molecular dynamics simulations to analyze the effect of surface wettability on the mass and heat transfer at the interface between water and (5,5) and (10,10) carbon CNTs. We firstly evaluated the contact angle of water on a single layer graphene applying the free energy perturbation approach with several Lennard-Jones parameters retrieved from the literature to model the cross-interactions. Then, we studied the spontaneous filling of water inside the CNTs, finding that the contact angle can be an adequate parameter to describe the water filling mechanisms if wettability is far from the hydrophilic-hydrophobic transition range. A more precise analysis shows that the increase in the value of the σ_{CO} Lennard-Jones parameter leads to a reduction in the accessible inner volume of the CNT and to a deepening of the potential well inside the tube, depending on the CNT curvature. For this reason, we introduced a new parameter (β as defined in the Eq. (9)) to take into account both the effect of wettability and CNT diameter. Given the complexity of the simulated setups, here we have limited the discussion of results to highlighting the correlation between the phenomenological parameter β and the observed filling response, whose validity has been proven for the considered configurations. Future works could focus, instead, on simpler Lennard-Jones fluids and/or exclude the nanotube edges from the analysis, therefore easing a more fundamental interpretation of numerical evidence and further generalize results.

Subsequently, we evaluated the thermal boundary resistance for the different Lennard-Jones parameters considered. The calculated thermal boundary resistance increases with the contact angle. This trend is justified considering the more structured layers of solid-like water obtained with lower contact angles, implying that hydrophilic conditions guarantee a better heat transfer between CNT and water. The heat transfer is eased (thermal boundary resis-

tance is reduced) in the hydrophilic regime, due to the presence of denser structured solid-like water.

In perspective, this work supports a more rational design of heat and mass transfer properties of CNT-based devices operating in nanothermal and nanobiological environments.

5. Supporting information

The Supporting Information is available free of charge online. The simulation setups used in this work are available at Zenodo archive associated with this work (<https://doi.org/10.5281/zenodo.7114607>).

Declaration of Competing Interest

The authors declare that they have no known competing financial interests or personal relationships that could have appeared to influence the work reported in this paper.

CRediT authorship contribution statement

Alessandro Casto: Methodology, Software, Validation, Formal analysis, Investigation, Data curation, Writing – original draft, Visualization. **Francesco Maria Bellussi:** Methodology, Software, Validation, Formal analysis, Writing – original draft, Visualization. **Michele Diego:** Formal analysis, Writing – review & editing, Supervision. **Natalia Del Fatti:** Formal analysis, Writing – review & editing, Supervision. **Francesco Banfi:** Conceptualization, Formal analysis, Writing – review & editing, Supervision. **Paolo Maioli:** Conceptualization, Formal analysis, Resources, Writing – review & editing, Supervision. **Matteo Fasano:** Conceptualization, Methodology, Formal analysis, Resources, Writing – review & editing, Supervision.

Data availability

Data will be made available on request.

Acknowledgments

A.C., F.M.B. and M.F. gratefully acknowledge the High Performance Computing Initiative of Politecnico di Torino (<http://hpc.polito.it/>) for the availability of computing resources and support. F.B. acknowledges financial support from CNRS through Délégation CNRS 2021–2022. M.D. acknowledges financial support by the LABEX iMUST (ANR-10-LABX-0064) of Université

de Lyon, within the program "Investissements d'Avenir" (ANR-11-IDEX-0007) operated by the French National Research Agency (ANR).

Supplementary material

Supplementary material associated with this article can be found, in the online version, at [10.1016/j.ijheatmasstransfer.2023.123868](https://doi.org/10.1016/j.ijheatmasstransfer.2023.123868)

References

- [1] S. Iijima, Helical microtubules of graphitic carbon, *Nature* 354 (1991) 56–58.
- [2] J.W. Mintmire, B.I. Dunlap, C.T. White, Are fullerene tubules metallic? *Phys. Rev. Lett.* 68 (1992) 631.
- [3] X. Chen, L. Zhang, M. Zheng, C. Park, X. Wang, C. Ke, Quantitative nanomechanical characterization of the van der Waals interfaces between carbon nanotubes and epoxy, *Carbon* 92 (2015) 214–228.
- [4] A.A. Balandin, Thermal properties of graphene and nanostructured carbon materials, *Nat. Mater.* 10 (2011) 569–581.
- [5] Z. Huang, T. Pan, M. Gao, Y. Lin, Chip cooling with carbon nanotube heat sink, in: 2014 15th International Conference on Electronic Packaging Technology, 2014, pp. 183–185.
- [6] M. Fasano, M.B. Bigdeli, Bottom up approach toward prediction of effective thermophysical properties of carbon-based nanofluids, *Heat Transfer Eng.* 39 (2018) 1686–1697.
- [7] O. Kolosov, A. Gruverman, J. Hatano, K. Takahashi, H. Tokumoto, Nanoscale visualization and control of ferroelectric domains by atomic force microscopy, *Phys. Rev. Lett.* 74 (1995) 4309.
- [8] M. Fasano, E. Chiavazzo, P. Asinari, Water transport control in carbon nanotube arrays, *Nanoscale Res. Lett.* 9 (2014) 559.
- [9] M. Fasano, A. Crisafulli, A. Cardellini, L. Bergamasco, E. Chiavazzo, P. Asinari, Thermally triggered nanorocket from double-walled carbon nanotube in water, *Mol. Simul.* 45 (2019) 417–424.
- [10] S. Kang, M. Pinault, L.D. Pfeiffer, M. Elimelech, Single-walled carbon nanotubes exhibit strong antimicrobial activity, *Langmuir* (2007) 8670–8673.
- [11] M.M. Noor, J. Goswami, V.A. Davis, Comparison of attachment and antibacterial activity of covalent and noncovalent lysozyme-functionalized single-walled carbon nanotubes, *ACS Omega* 5 (2020) 2254–2259.
- [12] J. Abraham, K.S. Vasu, C.D. Williams, K. Gopinadhan, Y. Su, C.T. Cherian, J. Dix, E. Prestat, S.J. Haigh, I.V. Grigorieva, et al., Tunable sieving of ions using graphene oxide membranes, *Nat. Nanotechnol.* 12 (2017) 546–550.
- [13] Y. Maniwa, H. Kataura, M. Abe, A. Udaka, S. Suzuki, Y. Achiba, H. Kira, K. Matsuda, H. Kadowaki, Y. Okabe, Ordered water inside carbon nanotubes: formation of pentagonal to octagonal ice-nanotubes, *Chem. Phys. Lett.* 401 (2005) 534–538.
- [14] A.I. Kolesnikov, J.-M. Zanotti, C.-K. Loong, P. Thiyagarajan, A.P. Moravsky, R.O. Loutfy, C.J. Burnham, Anomalous soft dynamics of water in a nanotube: a revelation of nanoscale confinement, *Phys. Rev. Lett.* 93 (2004) 035503.
- [15] M. Majumder, N. Chopra, R. Andrews, B.J. Hinds, Enhanced flow in carbon nanotubes, *Nature* 438 (2005). 44–44
- [16] L. Bergamasco, M. Morciano, M. Fasano, Effect of water nanoconfinement on the dynamic properties of paramagnetic colloidal complexes, *PCCP* 23 (2021) 16948–16957.
- [17] M.H. Köhler, J.R. Bordin, C.F. de Matos, M.C. Barbosa, Water in nanotubes: the surface effect, *Chem. Eng. Sci.* 203 (2019) 54–67.
- [18] E. Chiavazzo, M. Fasano, P. Asinari, P. Decuzzi, Scaling behaviour for the water transport in nanoconfined geometries, *Nat. Commun.* 5 (2014) 3565.
- [19] H. Dang, D. Song, Z. Lin, M. An, W. Ma, X. Zhang, Effect of axial electric field on confined water in carbon nanotube: enhancement of thermophoresis, *Int. J. Heat Mass Transf.* 190 (2022) 122751.
- [20] M. Diego, M. Gandolfi, A. Casto, F.M. Bellussi, F. Violla, A. Crut, S. Roddaro, M. Fasano, F. Vallée, N.D. Fatti, et al., Ultrafast nano generation of acoustic waves in water via a single carbon nanotube, *Photoacoustics* 28 (2022) 100407.
- [21] A. Alexiadis, S. Kassinos, The density of water in carbon nanotubes, *Chem. Eng. Sci.* 63 (2008) 2047–2056.
- [22] P. Pugliese, M. Conde, M. Rovere, P. Gallo, Freezing temperatures, ice nanotubes structures, and proton ordering of tip4p/ice water inside single wall carbon nanotubes, *J. Phys. Chem. B* 121 (2017) 10371–10381.
- [23] J. Abascal, E. Sanz, R.G. Fernández, C. Vega, A potential model for the study of ices and amorphous water: tip4p/ice, *J. Chem. Phys.* 122 (2005) 234511.
- [24] T. Werder, J.H. Walther, R. Jaffe, T. Halicioglu, P. Koumoutsakos, On the water-carbon interaction for use in molecular dynamics simulations of graphite and carbon nanotubes, *J. Phys. Chem. B* 107 (2003) 1345–1352.
- [25] F. Taherian, V. Marcon, N.F. van der Vegt, F. Leroy, What is the contact angle of water on graphene? *Langmuir* 29 (2013) 1457–1465.
- [26] L.A. Belyaeva, G.F. Schneider, Wettability of graphene, *Surf. Sci. Rep.* 75 (2020) 100482.
- [27] D.G. Cahill, W.K. Ford, K.E. Goodson, G.D. Mahan, A. Majumdar, H.J. Maris, R. Merlin, S.R. Phillpot, Nanoscale thermal transport, *J. Appl. Phys.* 93 (2003) 793–818.
- [28] D.G. Cahill, P.V. Braun, G. Chen, D.R. Clarke, S. Fan, K.E. Goodson, P. Keblinski, W.P. King, G.D. Mahan, A. Majumdar, et al., Nanoscale thermal transport. ii. 2003–2012, *Appl. Phys. Rev.* 1 (2014) 011305.
- [29] B. Tang, G. Hu, H. Gao, L. Hai, Application of graphene as filler to improve thermal transport property of epoxy resin for thermal interface materials, *Int. J. Heat Mass Transf.* 85 (2015) 420–429.
- [30] W. Evans, R. Prasher, J. Fish, P. Meakin, P. Phelan, P. Keblinski, Effect of aggregation and interfacial thermal resistance on thermal conductivity of nanocomposites and colloidal nanofluids, *Int. J. Heat Mass Transf.* 51 (2008) 1431–1438.
- [31] I.M. Khalatnikov, An introduction to the theory of superfluidity, CRC Press, 2018.
- [32] E.T. Swartz, R.O. Pohl, Thermal boundary resistance, *Rev. Mod. Phys.* 61 (1989) 605.
- [33] X. Wei, T. Zhang, T. Luo, Thermal energy transport across hard–soft interfaces, *ACS Energy Lett.* 2 (2017) 2283–2292.
- [34] S. Alosious, S.K. Kannam, S.P. Sathian, B. Todd, Prediction of kapitza resistance at fluid–solid interfaces, *J. Chem. Phys.* 151 (2019) 194502.
- [35] S. Alosious, S.K. Kannam, S.P. Sathian, B. Todd, Kapitza resistance at water–graphene interfaces, *J. Chem. Phys.* 152 (2020) 224703.
- [36] D. Alexeev, J. Chen, J.H. Walther, K.P. Giapis, P. Koumoutsakos, Kapitza resistance between few-layer graphene and water: liquid layering effects, *Nano Lett.* 15 (2015) 5744–5749.
- [37] R.E. Jones, J. Duda, X. Zhou, C. Kimmer, P. Hopkins, Investigation of size and electronic effects on kapitza conductance with non-equilibrium molecular dynamics, *Appl. Phys. Lett.* 102 (2013) 183119.
- [38] Z. Liang, P. Keblinski, Finite-size effects on molecular dynamics interfacial thermal-resistance predictions, *Phys. Rev. B* 90 (2014) 075411.
- [39] Z. Liang, M. Hu, Tutorial: determination of thermal boundary resistance by molecular dynamics simulations, *J. Appl. Phys.* 123 (2018) 191101.
- [40] C. Caddeo, C. Melis, A. Ronchi, C. Giannetti, G. Ferrini, R. Rurali, L. Colombo, F. Banfi, Thermal boundary resistance from transient nanocalorimetry: a multiscale modeling approach, *Phys. Rev. B* 95 (2017) 085306.
- [41] S.M. Nejad, R. Srivastava, F.M. Bellussi, H.C. Thielemann, P. Asinari, M. Fasano, Nanoscale thermal properties of carbon nanotubes/epoxy composites by atomistic simulations, *Int. J. Therm. Sci.* 159 (2021) 106588.
- [42] E. Lampin, Q.-H. Nguyen, P. Francioso, F. Cleri, Thermal boundary resistance at silicon–silica interfaces by molecular dynamics simulations, *Appl. Phys. Lett.* 100 (2012) 131906.
- [43] K.R. Hahn, M. Puligheddu, L. Colombo, Thermal boundary resistance at si/ge interfaces determined by approach-to-equilibrium molecular dynamics simulations, *Phys. Rev. B* 91 (2015) 195313.
- [44] F.M. Bellussi, C.S. Ezquerro, M. Laspalas, A. Chiminelli, Effects of graphene oxidation on interaction energy and interfacial thermal conductivity of polymer nanocomposite: a molecular dynamics approach, *Nanomaterials* 11 (2021) 1709.
- [45] L. Qiu, N. Zhu, Y. Feng, X. Zhang, X. Wang, Interfacial thermal transport properties of polyurethane/carbon nanotube hybrid composites, *Int. J. Heat Mass Transf.* 152 (2020) 119565.
- [46] F. Jabbari, A. Rajabpour, S. Saedodin, S. Wongwises, Effect of water/carbon interaction strength on interfacial thermal resistance and the surrounding molecular nanolayer of cnt and graphene flake, *J. Mol. Liq.* 282 (2019) 197–204.
- [47] N. Adam, Use of the term 'young's equation' for contact angles, *Nature* 180 (1957) 809–810.
- [48] F.M. Bellussi, O.M. Roscioni, M. Ricci, M. Fasano, Anisotropic electrostatic interactions in coarse-grained water models to enhance the accuracy and speed-up factor of mesoscopic simulations, *J. Phys. Chem. B* 125 (2021) 12020–12027.
- [49] F. Leroy, F. Müller-Plathe, Dry-surface simulation method for the determination of the work of adhesion of solid–liquid interfaces, *Langmuir* 31 (2015) 8335–8345.
- [50] A. Cardellini, F. Maria Bellussi, E. Rossi, L. Chiavarini, C. Becker, D. Cant, P. Asinari, M. Sebastiani, Integrated molecular dynamics and experimental approach to characterize low-free-energy perfluoro-decyl-acrylate (pfda) coated silicon, *Mater. Des.* 208 (2021) 109902.
- [51] B. Mortazavi, O. Benzerara, H. Meyer, J. Bardou, S. Ahzi, Combined molecular dynamics-finite element multiscale modeling of thermal conduction in graphene epoxy nanocomposites, *Carbon* N Y 60 (2013) 356–365.
- [52] A.P. Thompson, H.M. Aktulga, R. Berger, D.S. Bolintineanu, W.M. Brown, P.S. Crozier, P.J. Veld, A. Kohlmeyer, S.G. Moore, T.D. Nguyen, et al., LAMMPS—a flexible simulation tool for particle-based materials modeling at the atomic, meso, and continuum scales, *Comput. Phys. Commun.* 271 (2022) 108171.
- [53] J. Tersoff, New empirical approach for the structure and energy of covalent systems, *Phys. Rev. B* 37 (1988) 6991.
- [54] H. Berendsen, J. Grigera, T. Straatsma, The missing term in effective pair potentials, *J. Phys. Chem.* 91 (1987) 6269–6271.
- [55] R.W. Hockney, J.W. Eastwood, Computer simulation using particles, CRC Press, 2021.
- [56] B.A. Kakade, V.K. Pillai, Tuning the wetting properties of multiwalled carbon nanotubes by surface functionalization, *J. Phys. Chem. C* 112 (2008) 3183–3186.
- [57] A.I. Aria, M. Gharib, Reversible tuning of the wettability of carbon nanotube arrays: the effect of ultraviolet/ozone and vacuum pyrolysis treatments, *Langmuir* 27 (2011) 9005–9011.
- [58] M. Hosseini, J. Azamat, H. Erfan-Niya, Water desalination through fluorine-functionalized nanoporous graphene oxide membranes, *Mater. Chem. Phys.* 223 (2019) 277–286.
- [59] C.C. Ong, R. Jose, M.S.M. Saheed, Atomic defects of graphene-carbon nanotubes impact on surface wettability, *Appl. Surf. Sci.* 567 (2021) 150803.

- [60] W.L. Jorgensen, D.S. Maxwell, J. Tirado-Rives, Development and testing of the opls all-atom force field on conformational energetics and properties of organic liquids, *J. Am. Chem. Soc.* 118 (1996) 11225–11236.
- [61] W. Humphrey, A. Dalke, K. Schulten, Vmd: visual molecular dynamics, *J. Mol. Graph.* 14 (1996) 33–38.
- [62] A.I. Jewett, D. Stelter, J. Lambert, S.M. Saladi, O.M. Roscioni, M. Ricci, L. Autin, M. Maritan, S.M. Bashusqeh, T. Keyes, et al., Moltemplate: a tool for coarse-grained modeling of complex biological matter and soft condensed matter physics, *J. Mol. Biol.* 433 (2021) 166841.
- [63] F.M. Bellussi, A. Casto, M. Fasano, Data for Water filling in carbon nanotubes with different wettability and implications on nanotube/water heat transfer via atomistic simulations, 2022, doi:10.5281/zenodo.7114607.
- [64] W. Shinoda, M. Shiga, M. Mikami, Rapid estimation of elastic constants by molecular dynamics simulation under constant stress, *Phys. Rev. B* 69 (2004) 134103.
- [65] T.C. Beutler, A.E. Mark, R.C. van Schaik, P.R. Gerber, W.F.V. Gunsteren, Avoiding singularities and numerical instabilities in free energy calculations based on molecular simulations, *Chem. Phys. Lett.* 222 (1994) 529–539.
- [66] R.N. Wenzel, Resistance of solid surfaces to wetting by water, *Ind. Eng. Chem.* 28 (1936) 988–994.
- [67] A.B.D. Cassie, S. Baxter, Wettability of porous surfaces, *Trans. Faraday Soc.* 40 (1944) 546–551.
- [68] H. Yaghoubi, M. Foroutan, Wettability of striped patterned mono- and multi-layer graphene supported on platinum, *Appl. Surf. Sci.* 500 (2020) 144002.
- [69] F.M. Bellussi, O.M. Roscioni, E. Rossi, A. Cardellini, M. Provenzano, L. Persichetti, V. Kudryavtseva, G. Sukhorukov, P. Asinari, M. Sebastiani, et al., Wettability of soft plga surfaces predicted by experimentally augmented atomistic models, *MRS Bull* 48 (2022) 1–10.
- [70] P. Yue, J.J. Feng, C. Liu, J. Shen, A diffuse-interface method for simulating two-phase flows of complex fluids, *J. Fluid Mech.* 515 (2004) 293–317.
- [71] M. Chiricotto, F. Martelli, G. Giunta, P. Carbone, Role of long-range electrostatic interactions and local topology of the hydrogen bond network in the wettability of fully and partially wetted single and multilayer graphene, *J. Phys. Chem. C* 125 (2021) 6367–6377.
- [72] F. Leroy, S. Liu, J. Zhang, Parametrizing nonbonded interactions from wetting experiments via the work of adhesion: example of water on graphene surfaces, *J. Phys. Chem. C* 119 (2015) 28470–28481.
- [73] T.A. Pascal, W.A. Goddard, Y. Jung, Entropy and the driving force for the filling of carbon nanotubes with water, *Proc. Natl. Acad. Sci.* 108 (2011) 11794–11798.
- [74] X. Ma, S. Cambré, W. Wenseleers, S.K. Doorn, H. Htoon, Quasiphase transition in a single file of water molecules encapsulated in (6, 5) carbon nanotubes observed by temperature-dependent photoluminescence spectroscopy, *Phys. Rev. Lett.* 118 (2017) 027402.
- [75] S. Alosious, S.K. Kannam, S.P. Sathian, B. Todd, Nanoconfinement effects on the kapitza resistance at water–cnt interfaces, *Langmuir* 37 (2021) 2355–2361.
- [76] B. Ramos-Alvarado, S. Kumar, G. Peterson, Solid–liquid thermal transport and its relationship with wettability and the interfacial liquid structure, *J. Phys. Chem. Lett.* 7 (2016) 3497–3501.
- [77] S. Murad, I.K. Puri, Molecular simulation of thermal transport across hydrophilic interfaces, *Chem. Phys. Lett.* 467 (2008) 110–113.
- [78] A.S. Tascini, J. Armstrong, E. Chiavazzo, M. Fasano, P. Asinari, F. Bresme, Thermal transport across nanoparticle–fluid interfaces: the interplay of interfacial curvature and nanoparticle–fluid interactions, *PCCP* 19 (2017) 3244–3253.
- [79] O. Gutiérrez-Varela, S. Merabia, R. Santamaria, Size-dependent effects of the thermal transport at gold nanoparticle–water interfaces, *J. Chem. Phys.* 157 (2022) 084702.